

Permeability evolution in fine-grained Aji granite during triaxial compression experiments

Kazumasa Sueyoshi¹, Ikuo Katayama², and Kazuki Sawayama¹

¹Kyoto University

²Hiroshima University

November 24, 2022

Abstract

Triaxial compression experiments were carried out on samples of fine-grained Aji granite to measure the evolution of permeability during deformation prior to failure under confining pressures of 20 and 40 MPa. During the initial stages of deformation, a small decrease in permeability was observed, due to the closure of pre-existing microcracks; permeability then increased with increasing differential stress. During deformation, permeability varied by up to two orders of magnitude, and we observed a small pressure dependence, with a larger variation observed at 20 MPa than at 40 MPa. This suggests that more cracks developed during brittle deformation under the lower confining pressure. The observed increase in permeability during our experiments was approximately proportional to inelastic volumetric strain, which corresponded to the volume of dilatant cracks. On the other hand, prior to brittle failure we observed a further increase in permeability that was greater than the inelastic volumetric strain, suggesting crack aperture opening accelerated at this stress level ($> \sim 80\%$).

1 **Permeability evolution in fine-grained Aji granite during triaxial**
2 **compression experiments**

3

4 Kazumasa Sueyoshi^{1*}, Ikuo Katayama² and Kazuki Sawayama¹

5 ¹Institute for Geothermal Sciences, Graduate School of Science, Kyoto University

6 3088-176, Noguchibaru, Beppu, Oita, Japan, 874-0903

7 ²Department of Earth and Planetary Systems Science, Hiroshima University

8 1-3-1 Kagamiyama, Higashi-Hiroshima, Japan, 739-8526

9

10 *corresponding author: Kazumasa Sueyoshi

11 Institute for Geothermal Sciences, Graduate School of Science, Kyoto University

12 3088-176, Noguchibaru, Beppu, Oita, Japan, 874-0903

13 E-mail: sueyoshi.kazumasa.3k@kyoto-u.ac.jp

14

15

16 **Abstract**

17 Triaxial compression experiments were carried out on samples of fine-grained Aji granite
18 to measure the evolution of permeability during deformation prior to failure under confining
19 pressures of 20 and 40 MPa. During the initial stages of deformation, a small decrease in
20 permeability was observed, due to the closure of pre-existing microcracks; permeability then
21 increased with increasing differential stress. During deformation, permeability varied by up to
22 two orders of magnitude, and we observed a small pressure dependence, with a larger variation
23 observed at 20 MPa than at 40 MPa. This suggests that more cracks developed during brittle
24 deformation under the lower confining pressure. The observed increase in permeability during
25 our experiments was approximately proportional to inelastic volumetric strain, which
26 corresponded to the volume of dilatant cracks. On the other hand, prior to brittle failure we
27 observed a further increase in permeability that was greater than the inelastic volumetric strain,
28 suggesting crack aperture opening accelerated at this stress level ($>\sim 80\%$).

29

30 **Keywords**

31 Permeability and porosity, Microstructure, Fracture and flow, Geomechanics

32

33 **1. Introduction**

34 Fluid flow in rocks plays a key role in various geological processes, including crustal
35 deformation (Byerlee 1975; Sibson 1996), fluid-induced seismicity (Talwani and Acree 1984),
36 and geothermal developments (Shapiro et al. 1997). Laboratory experiments on rock samples
37 have yielded a wide range of permeabilities (10^{-12} to 10^{-23} m²) that are controlled by lithology,
38 porosity and pore geometry (Gueguen and Palciauskas 1994). Under hydrostatic conditions, an
39 increase in pressure reduces permeability through the progressive closure of pores within a rock
40 (Brace et al. 1968; Fortin et al. 2011). During deformations of porous rocks such as sandstone,
41 permeability consistently decreases due to the inelastic compaction through grain crushing and
42 pore collapse (Zhu and Wong 1997; Baud et al. 2012). In contrast, brittle deformation of
43 crystalline rocks such as granite can rapidly enhance permeability and affect fluid flow
44 processes. Although a small decrease in permeability occurs upon the application of small
45 stresses., a further increase in stress results in a marked increase in permeability as the rock
46 approaches failure (Zoback and Byerlee 1975; Mitchell and Faulkner 2008). These stress-
47 induced permeability variations are accompanied by dilatancy related to microcrack nucleation
48 and growth. Therefore, the development of microcracks during deformation is of great
49 importance in characterizing subsurface fluid flow.

50 In previous experiments, permeability was measured using the pulse transient technique,
51 which requires the interruption of deformation to make measurements (Zoback and Byerlee
52 1975). This may induce a relaxation of the axial loading stress and the permeability may be
53 affected, particularly during the dilatant stage. Mitchell and Faulkner (2008) measured the
54 permeability evolution of Westerly granite during continuous triaxial compression using the
55 pressure oscillation technique with water as a pore fluid. However, the high fluid viscosity
56 required a relatively large response time to achieve equilibrium of permeability during
57 deformation. In the present study, we measure permeability continuously during triaxial

58 compression using a gas flow method, in which the flux of gas, which is sensitive to the
59 presence of deformation microstructures, was monitored. We used nitrogen gas because it is
60 chemically inert, thereby preventing geochemical interaction and ensuring that the observed
61 variation in permeability results exclusively from mechanical processes.

62

63 **2. Experimental methods**

64 For our experiments, we used sample of fine-grained granite from Aji, Japan. The average
65 grain size of Aji granite is 0.3 mm, and it comprises 30 % quartz, 37 % plagioclase, 24 % K-
66 feldspar, and 8 % biotite (Kudo et al. 1992). The samples have a bulk density of 2.66 g/cm³ and
67 an apparent initial porosity of 0.62 % (Yukutake 1989). Based on elastic wave velocity
68 measurements, textures within the Aji granite are regarded to be near-isotropic (Watanabe and
69 Higuchi 2015). Each sample was prepared as a cylindrical shape with a diameter of 20 mm and
70 a length of 40 mm (uncertainty <0.05 mm). The samples were then enclosed in polyolefin tubes
71 to prevent interaction with the confining oil.

72 Triaxial deformation tests were performed using an intra-vessel deformation fluid-flow
73 apparatus at Hiroshima University. The axial piston was advanced at a constant rate and the
74 confining pressure was kept constant using a servo-controlled system (Fig. 1). We performed
75 multiple experiments under confining pressures of 20 and 40 MPa, and displacement rates of
76 0.04 and 0.02 mm/min. Our machine lacks a high-resolution feedback system to control post-
77 failure processes, and we therefore focus on the evolution of permeability until the attainment
78 of maximum differential stress.

79 Permeability was measured during deformation by a gas flow method using nitrogen gas
80 as a pore fluid, in which a constant upstream pore pressure was maintained ($P_p = 1.5$ MPa). To
81 achieve steady-state fluid flow during the initial stages of deformation, the desired pore pressure
82 was applied an hour before the deformation was conducted. Permeability (k) was determined

83 from the flow rate as follows:

$$84 \quad k = \frac{\mu}{A} \frac{L}{P_1 - P_2} \bar{Q}, \quad (1)$$

85 where μ is the viscosity of the pore fluid, P_1 is the upstream pore pressure, P_2 is the
86 downstream pore pressure (atmospheric pressure), A and L are the cross-sectional area and
87 length of the sample, respectively, and \bar{Q} is the mean flow rate as measured by a digital flow
88 meter (Tanikawa et al. 2008). During these calculations, we applied a correction to the pore
89 fluid volume to account for the compressibility of nitrogen gas. Although changes in gas flow
90 rate occur adjacent to pore walls, which results in pore pressure dependent permeability (i.e.,
91 Klinkenberg effect), we focus on the relative change in gas permeability under a constant pore
92 pressure gradient.

93 We measured strain in sample during deformation using double-cross strain gauges.
94 Volumetric strain (ε_v) was obtained from the axial (ε_a) and lateral strain (ε_r) as follows:

$$95 \quad \varepsilon_v = \varepsilon_a + 2\varepsilon_r. \quad (2)$$

96 During the initial stages of deformation, volumetric strain varied linearly with applied
97 differential stress. However, at stresses approaching the strength of the sample, non-linear
98 behavior was observed during dilation of the samples due to the development of microcracks.
99 As transport properties are influenced by the formation and connection of pores, we discuss the
100 relationship between permeability and inelastic volumetric strain during deformation.

101

102 **3. Results**

103 Experimental conditions and results are listed in Table 1. Permeabilities prior to
104 deformation ranged from $1.1 \times 10^{-19} \text{ m}^2$ to $2.6 \times 10^{-19} \text{ m}^2$, showing a small pressure
105 dependence, with higher permeabilities observed at the lower confining pressure (20 MPa).

106 Figure 2 shows stress-strain curves for experiments conducted under confining pressures

107 of 20 and 40 MPa. We use positive strain to represent compression and negative for extension.
108 The maximum differential stress varied with confining pressure, with experiments at high
109 confining pressure (40 MPa) producing higher differential stresses than those at 20 MPa. Under
110 both confining pressures, stress-strain behavior was linear-elastic during the initial stages of
111 deformation and became non-linear under higher differential stress. This non-linear relationship
112 prior to failure is typical behavior during brittle deformation, and reflects the development of
113 microcracks in the samples. This process is referred to as dilatancy, and the volume is observed
114 to increase during inelastic deformation. We determined the onset of dilatancy by following the
115 method of Brace et al. (1966). The results indicate that dilatancy began at ~40% of the
116 maximum differential stress, above which inelastic volumetric strain increased further as the
117 stress increased. When approaching macroscopic failure, a reversal of stress–volumetric strain
118 curve was observed at the stress level 62–77% of the maximum value. This stress threshold
119 (termed “crack damage stress”) corresponds to the point of the maximum volumetric strain
120 where unstable crack growth initiates (Bieniawski, 1967).

121 Figure 3 shows permeability results for our experiments under confining pressures of 20
122 and 40 MPa. In all experiments, permeability initially decreased due to the closure of pre-
123 existing cracks, and then increased under higher differential stress. Approaching the maximum
124 differential stress, a more pronounced increase in permeability was observed. At the maximum
125 differential stress, permeabilities were $0.4\text{--}2.3 \times 10^{-17} \text{ m}^2$ and $1.6\text{--}3.9 \times 10^{-18} \text{ m}^2$ at 20 and
126 40 MPa, respectively, and the maximum increase in permeability during deformation was
127 approximately two orders of magnitude. The variation in permeability was larger at 20 MPa
128 than at 40 MPa. Although most experiments were conducted at a constant displacement rate of
129 0.04 mm/min (strain-rate of $\sim 1.7 \times 10^{-5} \text{ s}^{-1}$), some runs were conducted at a slower rate of
130 0.02 mm/min; these experiments showed a similar evolution of permeability (Fig. 2). After
131 reached the maximum differential stress, permeability continued to increase until macroscopic

132 failure. However, quantitative measurement of this stage was prevented because the axial load
133 was not controlled by a servo-system, and brittle fracture occurred rapidly.

134

135 **4. Discussion**

136 ***4.1. Comparison with previous experiments***

137 Our experiments yielded systematic changes in permeability during brittle deformation,
138 and we first compare our results with previous experiments. Pioneering experiments by Zoback
139 and Byerlee (1975) investigated the permeability evolution during triaxial deformation of
140 Westerly granite samples. During loading, their results are similar to those presented here (Fig.
141 4a). However, their experiments were cycled and did not reach macroscopic failure, and hence
142 variations in permeability were limited to a factor of four, much less than those found in our
143 experiments until failure occurred. Mitchell and Faulkner (2008) measured the permeability of
144 Westerly granite samples using a pore pressure oscillation technique at effective confining
145 pressures of 10, 15, and 20 MPa. They observed a continuous increase in permeability after
146 reaching approximately half of the maximum differential stress; however, in contrast to our
147 experiments, an initial transient decrease in permeability related to the closure of pre-existing
148 cracks was not clearly observed (Fig. 4b). This difference likely resulted from their use of water
149 as a pore fluid, which has a higher viscosity than nitrogen gas, thereby limiting flow through
150 the narrow cracks during initial stage of loading. Fortin et al. (2011) reported similar behavior
151 during triaxial deformation of basaltic rocks (an initial decrease in permeability followed by an
152 increase approaching failure), but the variation was less than a factor of three, likely due to
153 competition between the closure of pre-existing cracks and the nucleation and growth of newly
154 formed vertical cracks.

155

156 ***4.2. Relationship between permeability and inelastic volumetric strain***

157 The inelastic behavior of the stress–volumetric strain relationship (i.e., dilatancy) initiates
158 ~40% of the maximum stress (C' in Fig. 5). As this dilatancy is related to the development of
159 microcracks, the increasing crack volume could enhance transport properties including
160 permeability. To explore the possible relationship between dilatancy and permeability during
161 deformation, we evaluated inelastic volumetric strain (D in Fig. 5) by subtracting an elastic
162 extrapolation from the measured volumetric strain.

163 Figure 6 shows the relative change in permeability and dilatancy as a function of the stress
164 level normalized by the maximum value. Permeability decreased slightly during the early stages
165 of deformation, and then began to increase at approximately half of the maximum differential
166 stress. This increase in permeability was accompanied by an increase in inelastic volumetric
167 strain. The change in permeability during this stage is attributed primarily to an increase in
168 dilatant crack porosity, considering that the inelastic volumetric strain corresponds to the crack
169 porosity. However, as samples approached brittle failure, permeability increased more rapidly
170 than inelastic volumetric strain. The differential stress at which the change in permeability
171 deviates from that of inelastic volumetric strain ~70–80% of the maximum stress. Therefore,
172 we infer that although permeability depends primarily on crack porosity, it is also influenced
173 by geometric factors (i.e., crack aperture) (Gueguen and Dienes, 1989; Sueyoshi et al., 2020).

174 One possible approach to estimating the contribution of crack geometric characteristics to
175 permeability is to clarify the power law between permeability (k) and porosity (ϕ) (Bernabe et
176 al., 2003):

$$177 \quad k \propto \phi^\alpha. \quad (3)$$

178 The slope α depends on the processes that lead to the evolution of the pore structure, and lies
179 between 1 and 2 during dilatant microcracking. According to Bernabe et al. (2003), this process
180 corresponds to the cooccurrence of the decrease in distance between cracks and the increase in
181 the crack aperture. Thus, microcrack evolution can be characterized by the stress level when α

182 exceeds 1, where the formation of a new crack and crack aperture dilation simultaneously
183 initiates. Based on the above, we estimated the changes in fluid flow characteristics during the
184 fracturing process from the relationship between the permeability and inelastic volumetric
185 strain, equivalent to the crack porosity in this study. Figure 7 shows representative results of the
186 permeability–inelastic volumetric strain curve on a log-log scale. Note that the inelastic
187 volumetric strain (D) was defined here after the stage of elastic deformation (i.e., the onset of
188 dilatancy), where the ratio of D to the ideal elastic volumetric strain (the dashed line in Fig. 5)
189 exceeds 3% (i.e., $D \sim 0.005$). The differential stresses at which the slopes exceed 1 are 71.7–
190 77.7% at a confining pressure of 20 MPa while 76.4–94.1% at that of 40 MPa (Figs. 7). These
191 results indicate that above these threshold stresses, the permeability rapidly increases due to the
192 concurrence of new crack formation (i.e., decrease in the distance between cracks) and crack
193 aperture dilation. As shown in Figure 6, the change in permeability deviates from that in the
194 inelastic volumetric strain at around 80% of the maximum stress, which can be caused by both
195 new crack formation and crack aperture opening. Although the slope α ranges from 0 to 1 during
196 the initial stage of inelastic deformation, this reflects the stable crack length increment less
197 contributing to permeability enhancement than the following crack growth.

198 Considering these results, we propose the deformation stage classifications in terms of the
199 permeability evolution processes (Fig. 8). In addition to the previous model (e.g., Paterson and
200 Wong, 2005), a new stage, the permeability enhancement stage, was newly defined in this study.
201 During *stage I*, a decrease in permeability is attributed to the closure of pre-existing cracks in
202 the direction perpendicular to the maximum principal stress. In this study, the permeability
203 reduction continued until the differential stress reached $\sim 20\%$ of the maximum value (Fig. 3).
204 *Stage II* is a stage of elastic behavior and is characterized by constant permeability. *Stage III* is
205 characterized by a slight permeability increase due to the initiation of the microcracking activity,
206 where this stage begins at $\sim 40\%$ of the maximum differential stress (Fig. 2). When the

207 differential stress is reached at the crack damage stress (62–77% of the maximum stress), the
208 volumetric strain turns from compression to dilation, indicating the onset of unstable crack
209 growth. The permeability enhancement behavior shows no significant changes yet at this stress.
210 As the differential stress increases further, the changing rate of permeability becomes much
211 larger than that of inelastic volumetric strain before reaching *Stage V* of macroscopic failure.
212 We defined *Stage IV* as the regime of significant permeability enhancement where new crack
213 formation and crack aperture dilation occur. The increase in the confining pressure may inhibit
214 the crack formation and dilation, although both the onset of dilatancy and crack damage stress
215 are less dependent on the confining pressure. The key feature of *stage IV* is dominant in aperture
216 increase, where we assume the new crack formation corresponds to the opening of grain
217 boundaries. On the other hand, *stage III* (the crack initiation stress and crack damage stress) can
218 be characterized by the stable and unstable growth of pre-existing crack length (Bieniawski
219 1967). The confining pressure is more likely to affect the crack aperture dilation than crack
220 length growth, resulting in the pressure dependence on the onset of *stage IV*. This is also
221 consistent with the experimental evidence that the crack aperture decreases with an increase in
222 confining pressure (Sueyoshi et al., 2020). We note that these experimental results established
223 the new relationship between permeability enhancement and microcracking behavior. To obtain
224 a more detailed permeability model, a quantitative analysis of the effects of geometric factors
225 such as crack connectivity and aperture during deformation is required.

226

227 **5. Conclusions**

228 This study presents experimental data on the continuous evolution of permeability during
229 triaxial compression. Using nitrogen gas as a pore fluid, we succeeded in measuring the
230 permeability of granite during deformation until failure occurred. In all experiments, as
231 differential stress increased, the permeability initially decreased due to the closure of pre-

232 existing cracks, and then began to increase at higher differential stress. Although permeability
233 increased by approximately two orders of magnitude during deformation, the variation was
234 larger at 20 MPa than at 40 MPa, suggesting that more cracks developed under the lower
235 confining pressure. Based on the relationship between inelastic volumetric strain and
236 permeability, permeability was controlled mainly by increases in crack porosity during the
237 initial stages of deformation, but a rapid increase in permeability prior to brittle failure was
238 controlled by both new crack formation and crack aperture enhancement. Since the crack
239 aperture is greatly influenced by the confining pressure, the higher the confining pressure, the
240 higher the stress level at which the permeability enhancement stage begins.

241

242 **Acknowledgments**

243 We thank Tadashi Yokoyama for discussions and technical advice on the experiments. This
244 study was supported by JSPS KAKENHI Grant Numbers 15H02147 and JP16H06476 in
245 Scientific Research on Innovative Areas “Science of Slow Earthquakes”.

246

247 **Data availability**

248 All datasets obtained or analyzed during this study are presented in this published paper.

249

250 **References**

251 Baud P., Meredith P. and Townend E., 2012. Permeability evolution during triaxial compaction

252 of an anisotropic porous sandstone, *J. geophys. Res.: Solid Earth*, 117(5), 1–23.

253 <https://doi.org/10.1029/2012JB009176>

254 Bernabé, Y., U. Mok, and B. Evans., 2003. Permeability-porosity relationships in rocks
255 subjected to various evolution processes, *Pure appl. Geophys.*, 160(5), 937-960.

256 <https://doi.org/10.1007/PL00012574>

257 Bieniawski, Z. T., 1967. Mechanism of brittle fracture of rock: part II—experimental
258 studies. *Int. J. Rock Mech. Min. Sci. Geomech. Abstr.*, 4(4), 407–423.
259 [https://doi.org/10.1016/0148-9062\(67\)90031-9](https://doi.org/10.1016/0148-9062(67)90031-9)

260 Brace W. F., Paulding B. W. and Scholz C., 1966. Dilatancy in the fracture of crystalline rocks,
261 *J. geophys. Res.*, 71(16), 3939–3953. <https://doi.org/10.1029/JZ071i016p03939>

262 Brace W. F., Walsh J. B., and Frangos W. T., 1968. Permeability of Granite under High Pressure,
263 *J. geophys. Res.*, 73(6), 2225–2236. <https://doi.org/10.1029/JB073i006p02225>

264 Byerlee J. D., 1975. The fracture strength and frictional strength of Weber Sandstone, *Int. J.*
265 *Rock Mech. Min. Sci.*, 12(1), 1–4. [https://doi.org/10.1016/0148-9062\(75\)90736-6](https://doi.org/10.1016/0148-9062(75)90736-6)

266 Fortin J., Stanchits S., Vinciguerra S., and Guéguen, Y., 2011. Influence of thermal and
267 mechanical cracks on permeability and elastic wave velocities in a basalt from Mt. Etna
268 volcano subjected to elevated pressure, *Tectonophysics*, 503(1–2), 60–74.
269 <https://doi.org/10.1016/j.tecto.2010.09.028>

270 Gueguen Y. and Dienes J., 1989. Transport Properties of Rocks from Statistics and Percolation,
271 *Math. Geol.*, 21(1), 1–13. <https://doi.org/10.1007/BF00897237>

272 Gueguen Y., and Palciauskas V., 1994. *Introduction to the Physics of Rocks*, Press, Princeton,
273 N.J.

274 Kudo Y., Sano O., Murashige N., Mizuta Y. and Nakagawa K., 1992. Stress-induced crack path
275 in Aji granite under tensile stress, *Pure appl. Geophys.*, 138(4), 641–656.
276 <https://doi.org/10.1007/BF00876342>

277 Lei, Xinglin., 2006. Typical phases of pre-failure damage in granitic rocks under differential
278 compression, *Geological Society, London, Special Publications*, 261(1), 11–29.
279 <https://doi.org/10.1144/GSL.SP.2006.261.01.02>

280 Mitchell T. M., and Faulkner D. R., 2008. Experimental measurements of permeability
281 evolution during triaxial compression of initially intact crystalline rocks and implications

282 for fluid flow in fault zones, *J. geophys. Res.: Solid Earth*, 113(11), 1–16.
283 <https://doi.org/10.1029/2008JB005588>

284 Paterson, Mervyn S., and Teng-fong Wong., 2005. *Experimental rock deformation-the brittle*
285 *field*, Springer Science & Business Media.

286 Scholz C. H., 1968. Microfracturing and the inelastic deformation of rock in compression, *J.*
287 *geophys. Res.*, 73(4), 1417-1432. <https://doi.org/10.1029/JB073i004p01417>

288 Shapiro S. a., Huenges E., and Borm G., 1997. Estimating the crust permeability from fluid-
289 injection-induced seismic emission at the KTB site, *Geophys. J. Int.*, 131(2), F15–F18.
290 <https://doi.org/10.1111/j.1365-246X.1997.tb01215.x>

291 Sibson R. H., 1996. Structural permeability of fluid-driven fault-fracture meshes, *J. Struct.*
292 *Geol.*, 18(8), 1031–1042. [https://doi.org/10.1016/0191-8141\(96\)00032-6](https://doi.org/10.1016/0191-8141(96)00032-6)

293 Sueyoshi, Kazumasa, Tadashi Yokoyama, and Ikuo Katayama., 2020. Experimental
294 measurement of the transport flow path aperture in thermally cracked granite and the
295 relationship between pore structure and permeability, *Geofluids*, 2020, 1-10.
296 <https://doi.org/10.1155/2020/8818293>

297 Talwani P., and Acree S., 1984. Pore pressure diffusion and the mechanism of reservoir-induced
298 seismicity, *Pure appl. Geophys.*, 122(6), 947–965. [https://doi.org/10.1007/978-3-0348-](https://doi.org/10.1007/978-3-0348-6245-5_14)
299 [6245-5_14](https://doi.org/10.1007/978-3-0348-6245-5_14)

300 Tanikawa W., Shimamoto T., Wey S. K., Lin C. W. and Lai W. C., 2008. Stratigraphic variation
301 of transport properties and overpressure development in the Western Foothills, Taiwan, *J.*
302 *geophys. Res.: Solid Earth*, 113(12), 1–17. <https://doi.org/10.1029/2008JB005647>

303 Watanabe T. and Higuchi A., 2015. Simultaneous measurements of elastic wave velocities and
304 electrical conductivity in a brine-saturated granitic rock under confining pressures and their
305 implication for interpretation of geophysical observations, *Prog. Earth Planet. Sci.*, 2(1),
306 37. <https://doi.org/10.1186/s40645-015-0067-0>

307 Yukutake H., 1989. Fracturing Process of Granite Inferred From Measurements of Spatial and
308 Temporal Variations in Velocity During Triaxial Deformations, *J. geophys. Res.*, 94,
309 15639–15651. <https://doi.org/10.1029/JB094iB11p15639>
310 Zhu W. and Wong T., 1997. The transition from brittle faulting to cataclastic flow: Permeability
311 evolution, *J. geophys. Res.: Solid Earth*, 102(B2), 3027–3041.
312 <https://doi.org/10.1029/96JB03282>
313 Zoback M. D., and Byerlee J. D., 1975. The effect of microcrack dilatancy on the permeability
314 of Westerly granite, *J. geophys. Res.*, 80(5), 752–755.
315 <https://doi.org/10.1029/JB080i005p00752>

316

317 **Figure captions**

318 **Figure 1.** Overview of the intra-vessel deformation fluid-flow apparatus.

319

320 **Figure 2.** Relationships among differential stress and axial strain (ϵ_a), radial strain (ϵ_r), and
321 volumetric strain (ϵ_v) of Aji granite under confining pressures of 20 and 40 MPa.
322 Compressive strain was taken as positive, and extensional strain as negative.

323

324 **Figure 3.** Evolution of permeability as a function of differential stress under confining pressures
325 of 20 (blue dots) and 40 MPa (red dots). The data points of IVA1389 and IVA1403
326 represent experiments conducted at a slower deformation rate of 0.02 mm/min. All
327 other data represent experiments conducted at a deformation rate of 0.04 mm/min.

328

329 **Figure 4.** Comparison of our experiment data with those of previous experimental studies. (a)
330 Experimental results at $P_c = 40$ MPa compared with the data of Zoback and Byerlee's⁸
331 experiment on Westerly granite at an effective pressure of 39 MPa, with permeability

332 measured by a pulse transient method using argon gas. (b) Experimental results at P_c
333 = 20 MPa compared with the data of Mitchell and Faulkner¹⁰ obtained from Westerly
334 granite at an effective pressure of 20 MPa, with permeability measured by a pore
335 pressure oscillation method using water as a pore fluid.

336

337 **Figure 5.** Typical relationship among differential stress and strains during triaxial compression
338 experiments of Aji granite samples at $P_c = 20$ MPa. The parameters C , C' , and D
339 represent the maximum differential stress, onset of dilatancy, and inelastic volumetric
340 strain, respectively. The dashed line represents the ideal elastic volumetric strain
341 extrapolated from 20–30% of the maximum differential stress.

342

343 **Figure 6.** Inelastic volumetric strain and permeability normalized to the initial values (k/k_{initial})
344 as functions of differential stress normalized to the maximum differential stress at P_c
345 = 20 (a) and 40 MPa (b).

346

347 **Figure 7.** Relationship between permeability normalized to the initial value and inelastic
348 volumetric strain at confining pressures of 20 and 40 MPa. Light blue square:
349 IVA1454; blue circle: IVA1451; light red square: IVA1471; red circle: IVA1428. Note
350 that strains were only measured for these four experiments.

351

352 **Figure 8.** Permeability as a function of inelastic volumetric strain at confining pressure of 20
353 (a – c) and 40 MPa (d – f). The straight lines represent the lines with slope 1 tangent
354 to the permeability – inelastic volumetric strain curve. The green plots indicate the
355 contact points of the tangent lines with slope 1.

356

357 **Figure 9.** Deformation stages during a triaxial compression test in terms of the permeability
358 evolution. (a) Typical changes in the differential stress normalized by the peak stress
359 and permeability as functions of axial strain at confining pressure of 20 MPa. (b)
360 Schematic illustrations of microcracking characteristics within a sample at each stage.

361

362 **Table caption**

363 **Table 1.** Summary of experimental conditions and results.

364 Pc: confining pressure; k_{initial} : initial permeability; k_{max} : permeability at maximum
365 differential stress.

366

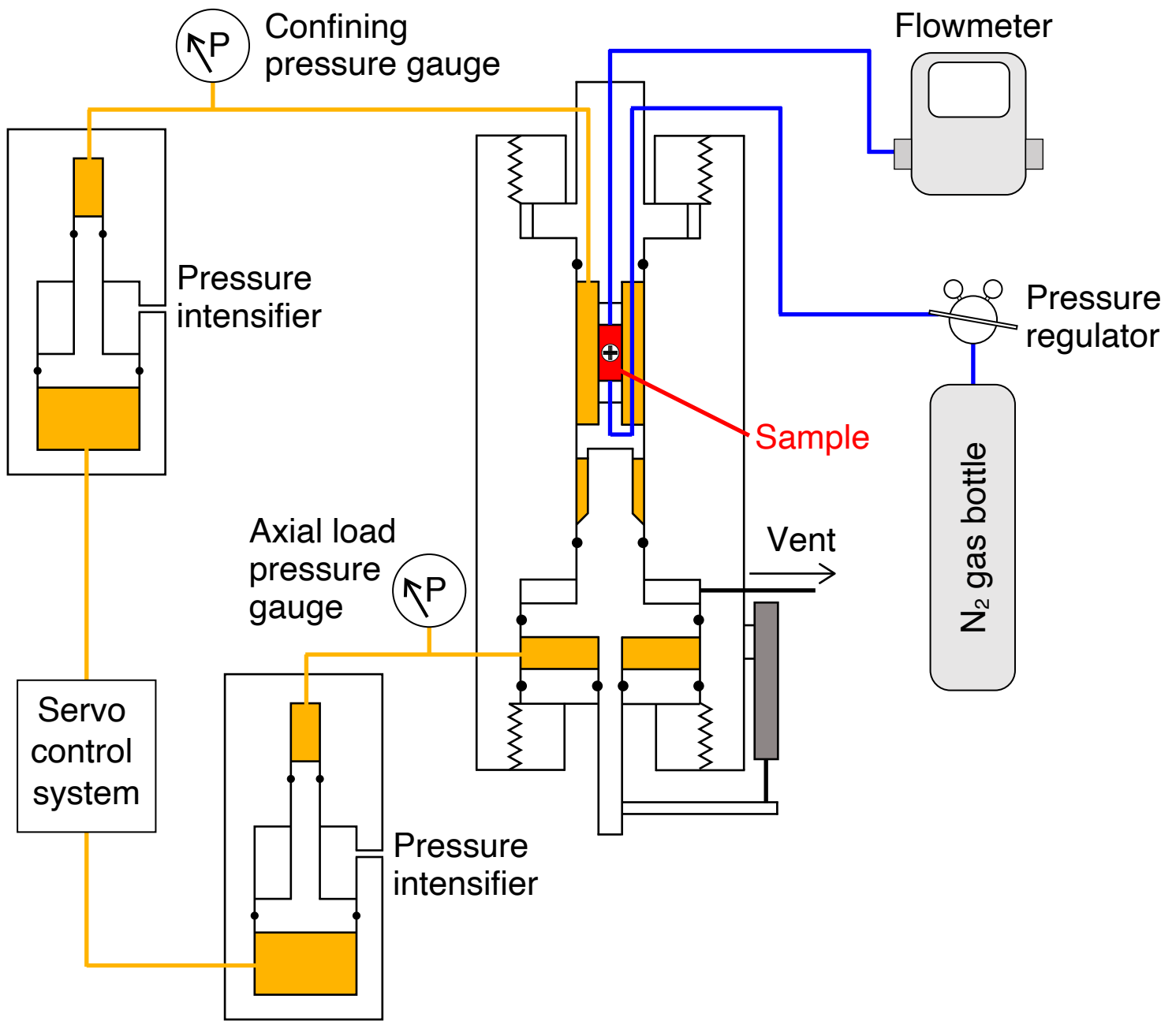


Figure 1

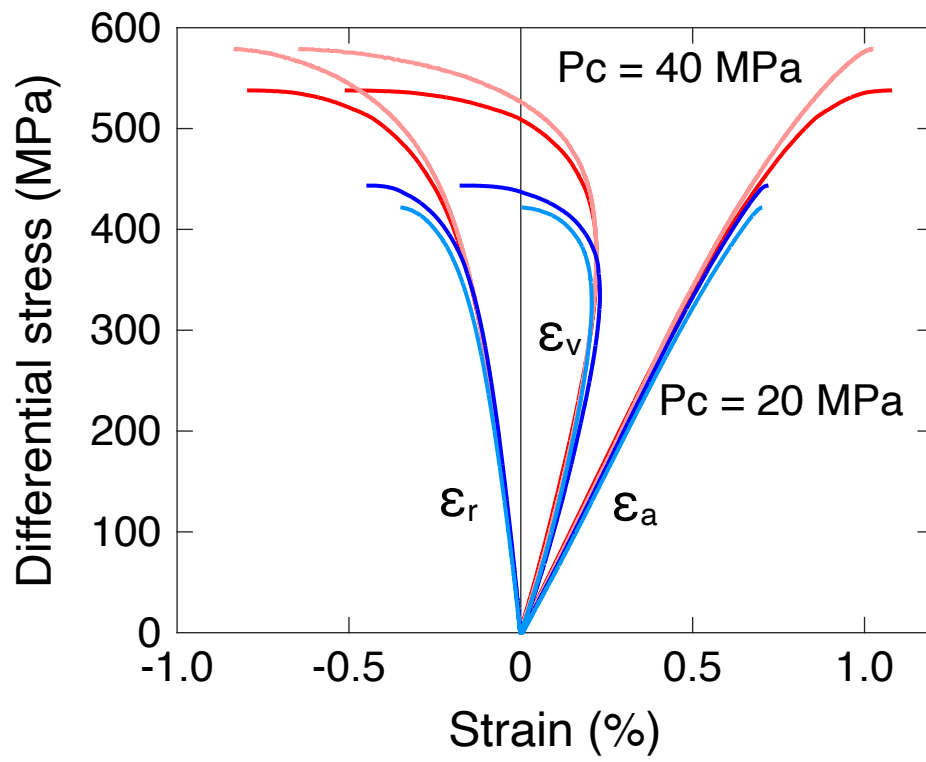


Figure 2

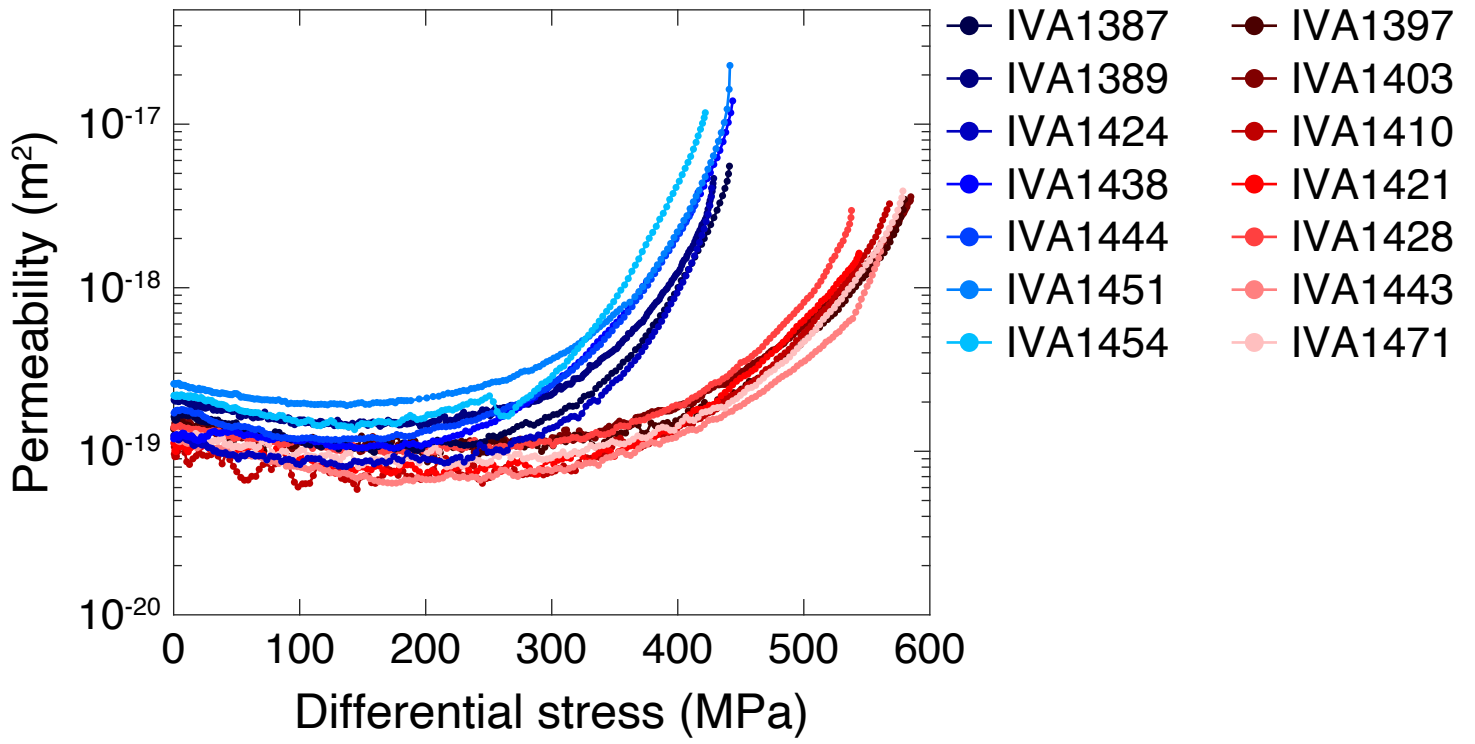


Figure 3

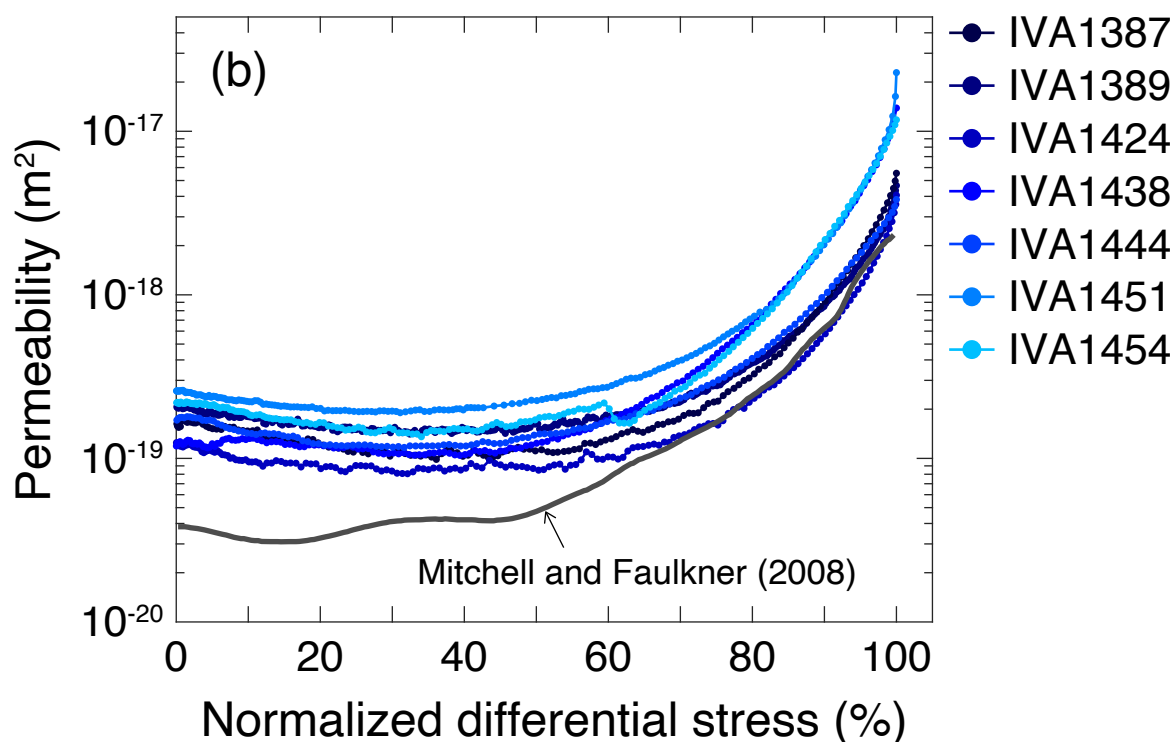
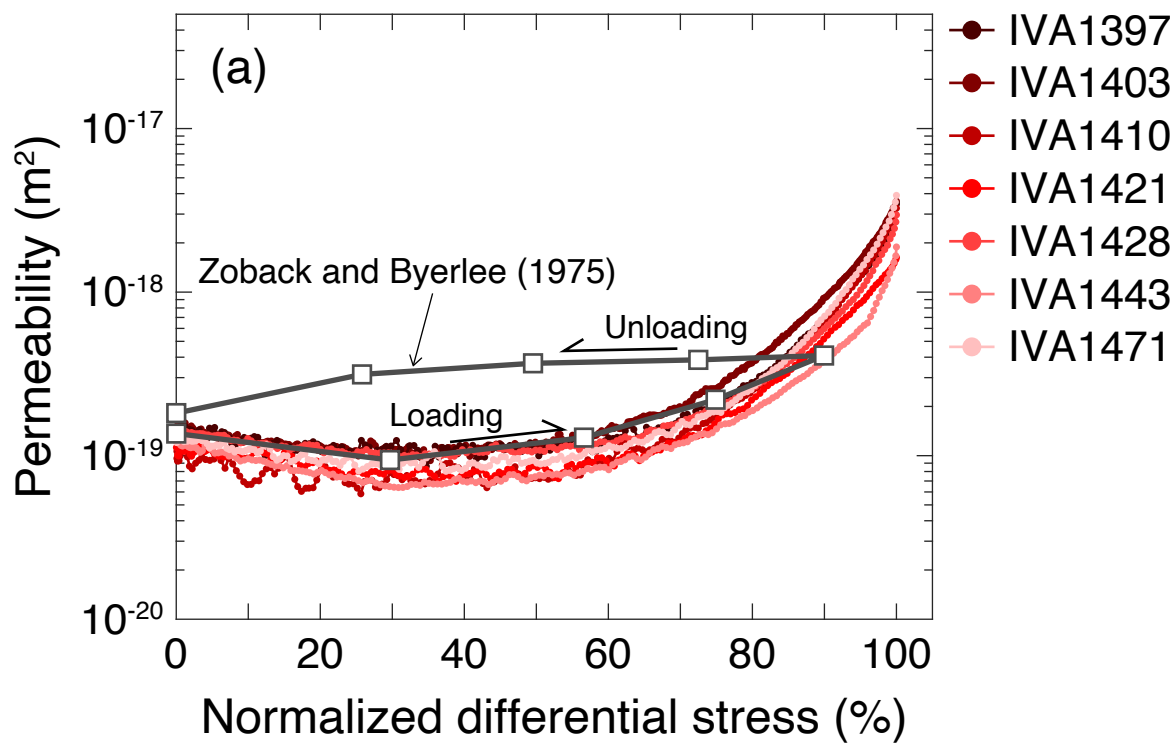


Figure 4

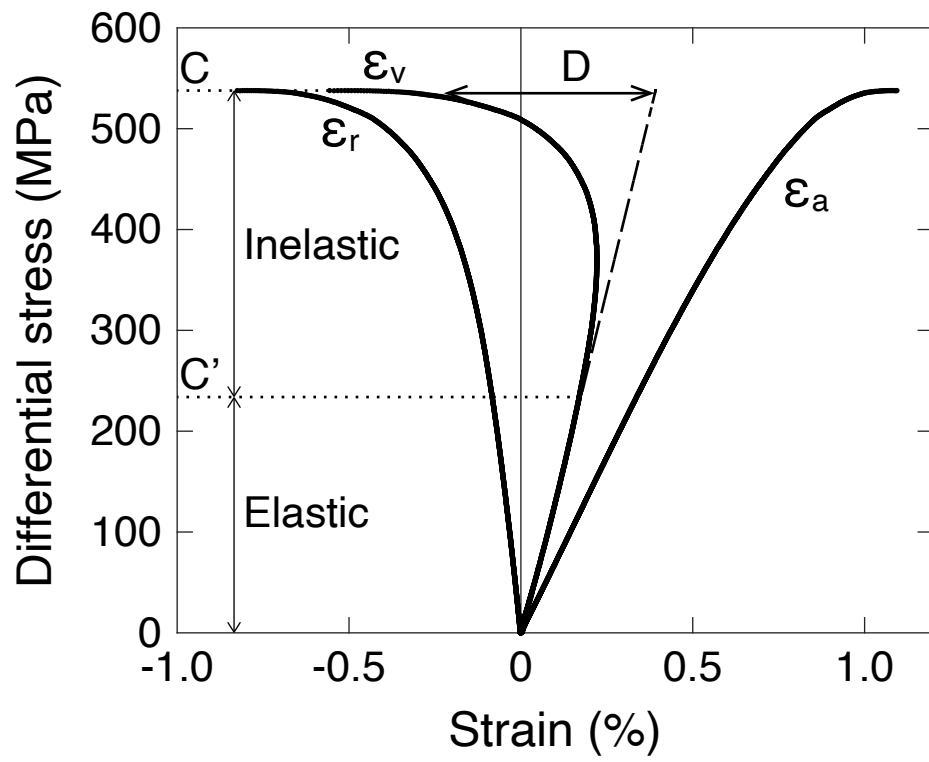


Figure 5

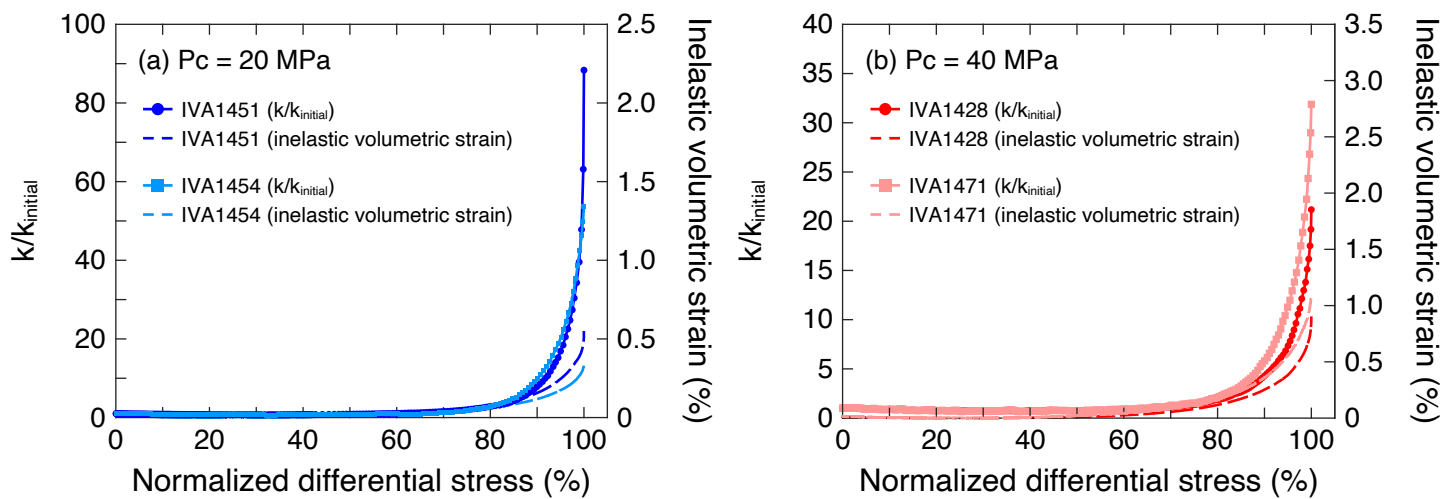


Figure 6

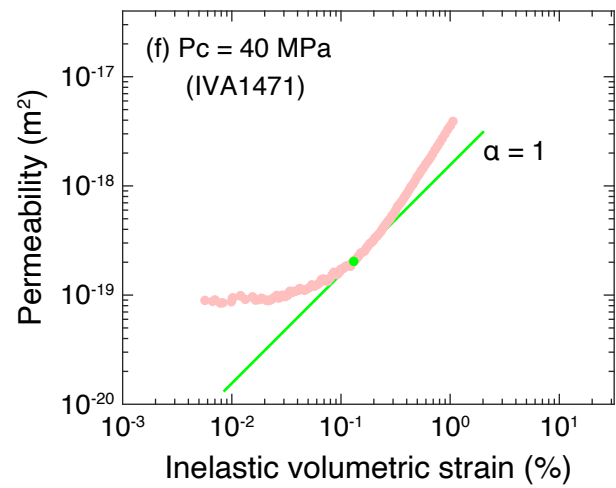
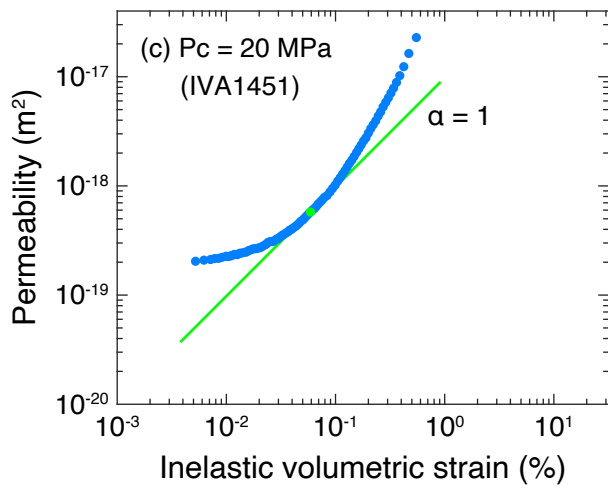
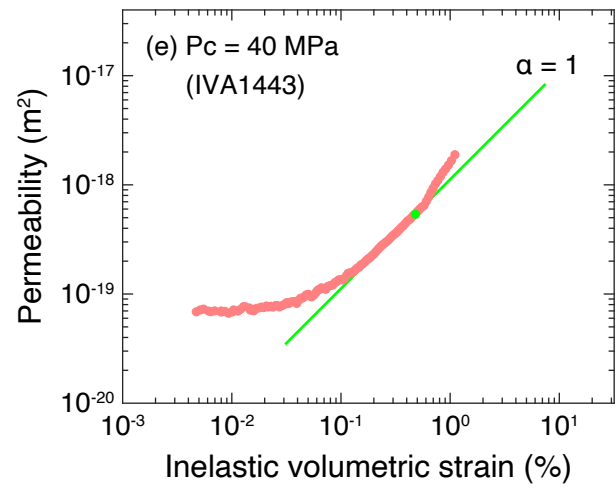
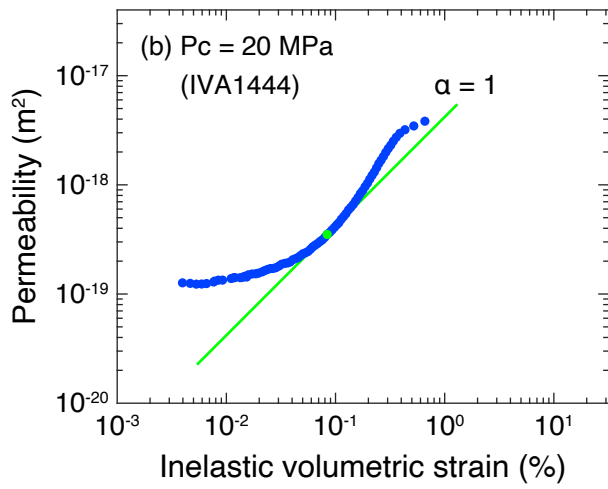
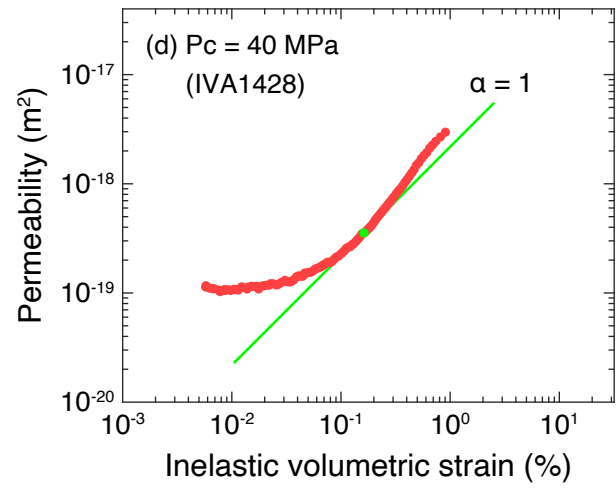
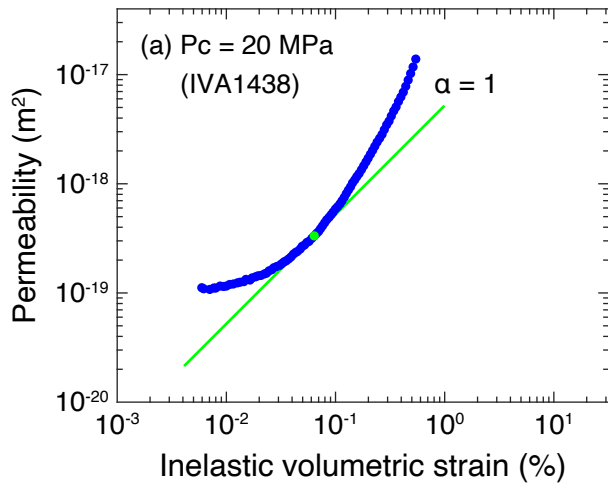


Figure 7

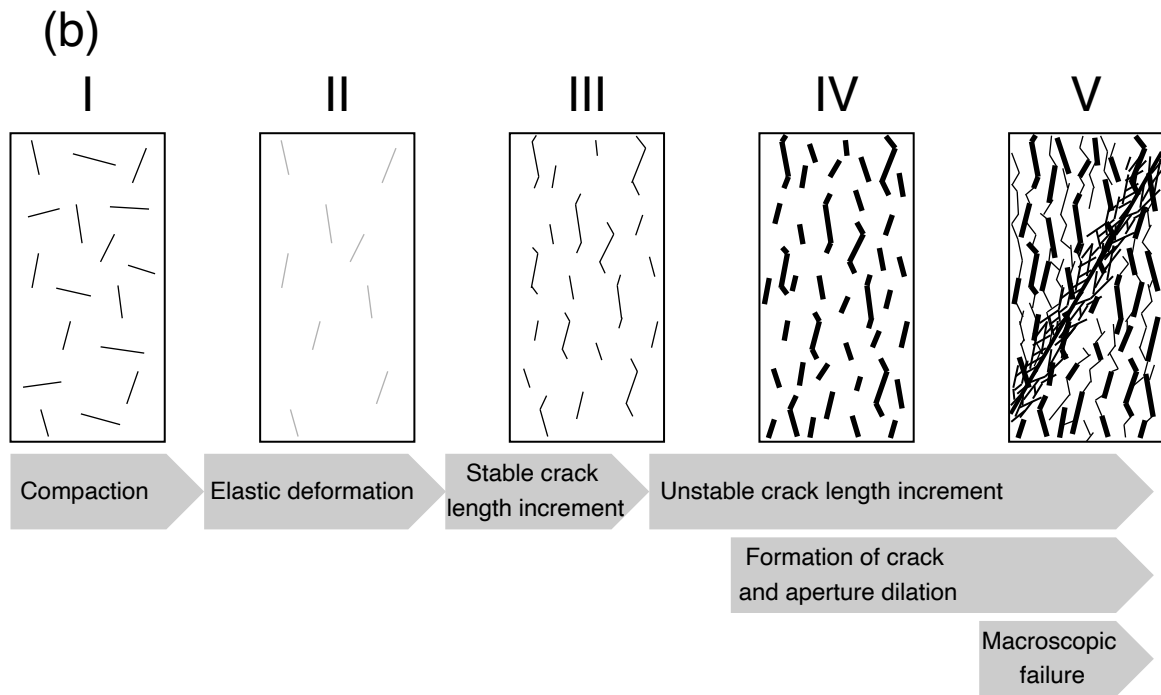
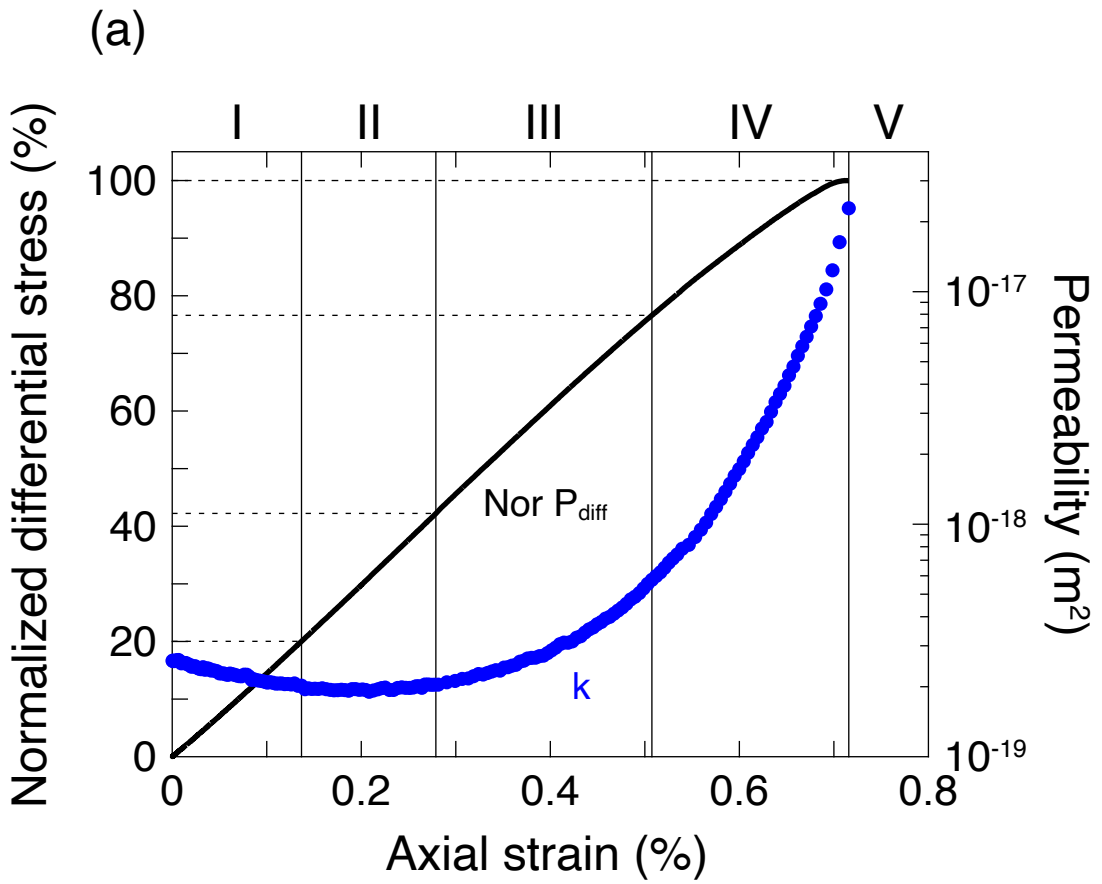


Figure 8

Table 1. Summary of experimental conditions and results

No.	Pc (MPa)	Displacement rate (mm/min)	Onset of dilatancy		Crack damage stress		Onset of <i>stage IV</i>		Maximum differential stress (MPa)	k _{initial} (m ²)	k _{max} (m ²)
			MPa	%	MPa	%	MPa	%			
IVA1387	20	0.04							441	1.63×10 ⁻¹⁹	5.54×10 ⁻¹⁸
IVA1389	20	0.02							428	2.06×10 ⁻¹⁹	4.66×10 ⁻¹⁸
IVA1424	20	0.04	162	37.9	265	62.1			427	1.25×10 ⁻¹⁹	4.06×10 ⁻¹⁸
IVA1438	20	0.04	187	42.2	302	68.2	318	71.7	444	1.19×10 ⁻¹⁹	1.39×10 ⁻¹⁷
IVA1444	20	0.04	176	42.3	282	67.8	323	77.7	416	1.71×10 ⁻¹⁹	3.83×10 ⁻¹⁸
IVA1451	20	0.04	186	42.2	330	74.7	338	76.6	441	2.59×10 ⁻¹⁹	2.28×10 ⁻¹⁷
IVA1454	20	0.04	176	41.6	326	77.3			422	2.19×10 ⁻¹⁹	1.17×10 ⁻¹⁷
IVA1397	40	0.04							580	1.37×10 ⁻¹⁹	3.47×10 ⁻¹⁸
IVA1403	40	0.02							585	1.48×10 ⁻¹⁹	3.60×10 ⁻¹⁸
IVA1410	40	0.04							568	1.06×10 ⁻¹⁹	3.26×10 ⁻¹⁸
IVA1421	40	0.04							544	1.12×10 ⁻¹⁹	1.63×10 ⁻¹⁸
IVA1428	40	0.04	234	43.5	370	68.7	453	84.2	538	1.40×10 ⁻¹⁹	2.97×10 ⁻¹⁸
IVA1443	40	0.04	213	38.0	362	64.6	528	94.1	561	1.21×10 ⁻¹⁹	1.89×10 ⁻¹⁸
IVA1471	40	0.04	234	40.3	374	64.6	443	76.4	579	1.22×10 ⁻¹⁹	3.90×10 ⁻¹⁸

Pc, confining pressure; k_{initial}, initial permeability; k_{max}, permeability at maximum differential stress.